NJC

New Journal of Chemistry

An international journal of the chemical sciences

www.rsc.org/njc

Volume 32 | Number 2 | February 2008 | Pages 181–368

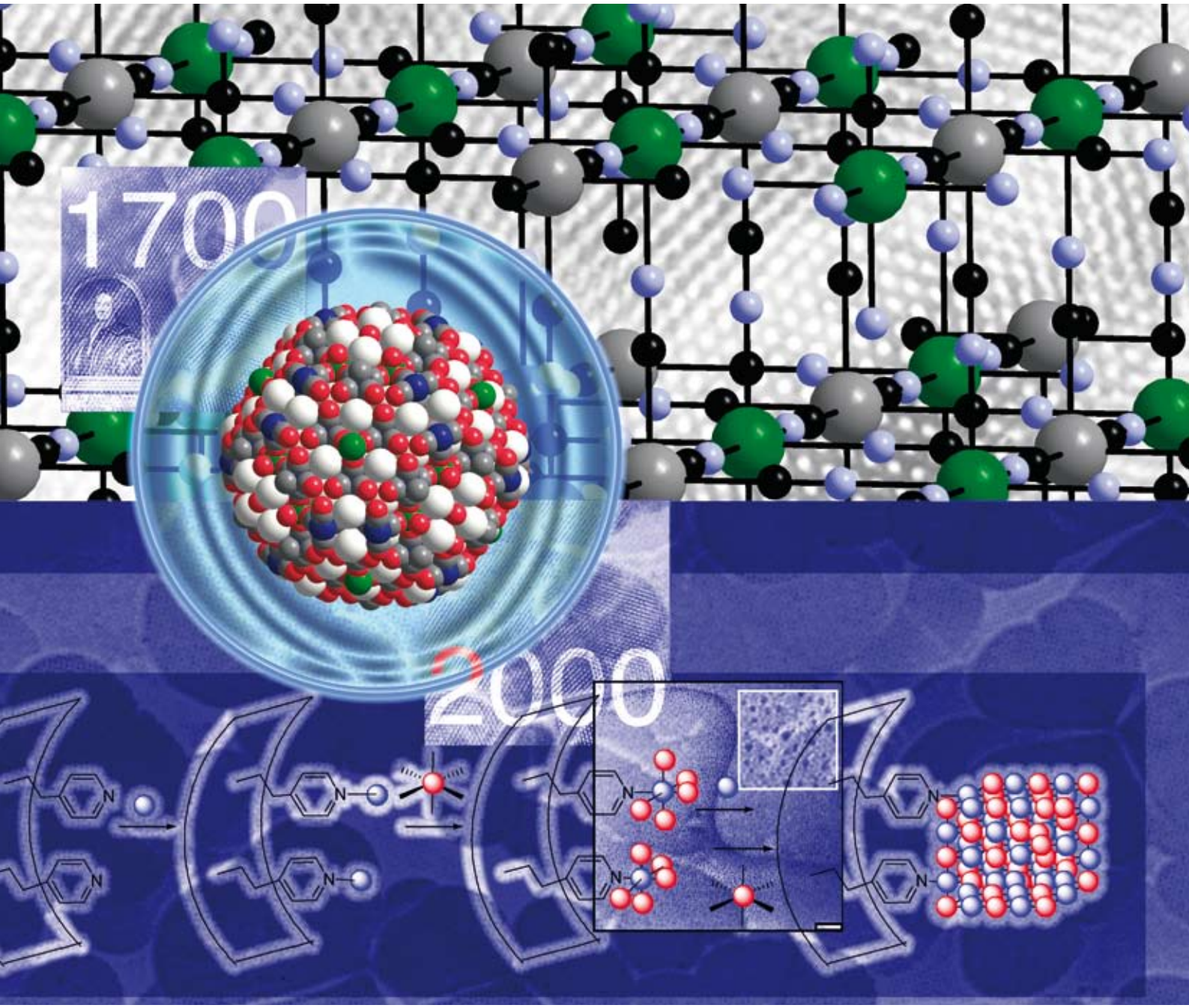

ISSN 1144-0546

RSC Publishing

CNRS CENTRE NATIONAL DE LA RECHERCHE SCIENTIFIQUE

PAPER

Joulia Larionova *et al.*

Synthesis and behaviour of size controlled cyano-bridged coordination polymer nanoparticles within hybrid mesoporous silica

1144-0546(2008)32:2;1-5

Synthesis and behaviour of size controlled cyano-bridged coordination polymer nanoparticles within hybrid mesoporous silica†

Benjamin Folch,[a] Yannick Guari,*[a] Joulia Larionova,*[a] Carlos Luna,[b] Claudio Sangregorio,*[b] Claudia Innocenti,[b] Andrea Caneschi[b] and Christian Guérin[a]

Received (in Montpellier, France) 22nd June 2007, Accepted 20th September 2007
First published as an Advance Article on the web 12th November 2007
DOI: 10.1039/b709490f

Size controlled cyano-bridged coordination polymer nanoparticles $M^{n+}/[M'(CN)_m]^{3-}$ (where M^{n+} = Ni^{2+}, Fe^{2+}, Co^{2+} and M' = Fe^{3+}, Co^{3+}(m = 6); Mo^{5+} (m = 8)) have been synthesised and organised by using mesostructured hybrid silica hosts of various sizes (3.4, 5.3 and 7.5 nm) containing $-(CH_2)_2C_5H_4N$ groups. The obtained composite materials were studied by transmission electronic microscopy (TEM), infrared and electronic spectroscopies, nitrogen sorption, X-ray diffraction and magnetic measurements. These analyses reveal the formation of hetero- or homo-metallic cyano-bridged nanoparticles with controlled stoichiometry uniform in size and shape within the silica matrix. The size of the nanoparticles is controlled by the pore size of the silica used. The magnetic study of these nanocomposite materials reveal an appearance of a spin-glass like regime which can be caused by a spin frustration on the surface of the nanoparticles and/or by interparticle magnetostatic interactions.

Introduction

Cyano-bridged homo- and hetero-metallic coordination polymers belong to an important family of molecule-based materials presenting interesting magnetic, optic, photo-switchable and intercalation properties.[1] These compounds may also be used as molecular sieves, as materials for hydrogen storage or as radioactive poison antidotes.[2] Consequently, during the last twenty years, numerous compounds of this family with various structures have been synthesised and extensively studied due to their fundamental interest as well as their technological applications.[3] More recently, the research activity was also devoted to the synthesis and studies of size and shape controlled cyano-bridged metallic coordination polymer materials at the nano-sized level regime.[4] It should be outlined that due to the very important surface/core atoms ratio or confinement effects, nanometer-scaled materials often exhibit an appearance of new interesting size-dependent physical and chemical properties, which can not be observed in their bulk analogous.[5] For this reason, such nano-sized materials are interesting candidates for applications in many fields, including electronics, catalysis, separation, biology, medical imagery and others.[6] However, their synthesis is rendered difficult due to the need of size, shape and surface state control of the nano-objects and the requirement of their organisation in space.

The first work on the synthesis of nanocrystals of Prussian Blue of 12–50 nm was reported by Mann and co-workers.[7] Henceforth, the number of articles devoted to the investigations of coordination nanopolymers is in constant expansion. Indeed, the synthesis of cyano-bridged metallic nanoparticles of different size by using reverse micelles,[8] polymer[9] and biopolymer,[10] amorphous silica[11] as matrices or ionic liquids as structuring media[12] were reported. In this connection, we recently reported a new approach to the synthesis and organisation of cyano-bridged coordination polymer nanoparticles based on hexa- and octa-cyanometallate building blocks by using hybrid mesostructured silica as matrix.[13] These nanoparticles were obtained by growing of the cyano-bridged metallic network at specific sites of hybrid mesostructured silica. The presence of pyridine functionalities provides chemical anchoring of the nanoparticles and allows the growth control inside the silica pores.

Such preliminary results encouraged us to further investigate these nanocomposite materials, extend this approach to other hetero- and homo-metallic cyano-bridged coordination nanopolymers and examine the possibility of size control over the nanoparticles. In the present work, we report on the synthesis and textural, structural and magnetic studies of a large range of cyano-bridged metallic coordination polymer

[a] *Institut Charles Gerhardt Montpellier, UMR 5253 CNRS-UM2-ENSCM-UM1, Chimie Moléculaire et Organisation du Solide, Université Montpellier II, Place E. Bataillon, 34095 Montpellier cedex 5, FranceE-mail: joulia@univ-montp2.fr, guari@univ-montp2.fr.; Fax: (33) 4 67 14 38 52*
[b] *INSTM Research Unit-Dipartimento di Chimica, Università di Firenze, via della Lastruccia 3, 50019 Sesto F.no Firenze, Italy. E-mail: claudio.sangregorio@unifi.it*

† Electronic supplementary information (ESI) available: Fig. 1S: Wt% of metal *vs.* number of $M^{n+}/[M'(CN)_m]^{3+}$ impregnation treatments for **2a** and **2b**. Fig. 2S: TEM image of **1a**. Fig. 3S: Nitrogen adsorption/desorption isotherms and BJH pore-size distributions. Fig. 4S: FC and ZFC curves for sample **3a** at an external magnetic field of 10 Oe. Fig. 5S: FC and ZFC curves for $Ni_3[Fe(CN)_6]_2{\cdot}13H_2O$ at an external magnetic field of 10 Oe. Fig. 6S: Temperature dependence of the in-phase and out-of-phase components of the ac susceptibility of **3a** with zero dc magnetic field. Fig. 7S: Temperature dependence of the in-phase and out-of-phase components of the ac susceptibility of **3b** with zero dc magnetic field. Fig. 8S: Temperature dependence of the in-phase and out-of-phase components of the ac susceptibility of $Ni_3[Fe(CN)_6]_2{\cdot}13H_2O$ with zero dc magnetic field. See DOI: 10.1039/b709490f

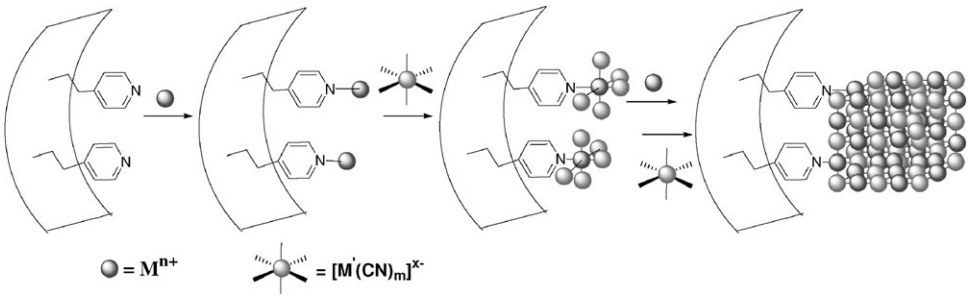

Scheme 1

nanoparticles with controlled stoichiometry, grown into hybrid SBA-15 and MCM-41 types mesostructured hexagonal silicas containing $-(CH_2)_2C_5H_4N$ functionalities and having different size of pores. We give a special emphasis on the relationship between the pore size of the silica matrix and the size of the nanoparticles and their size-dependent magnetic properties (Scheme 1).

Results and discussion

Synthesis

The scheme represents the method that we used in order to form and organize the coordination polymer nanoparticles into mesostructured hybrid silica. It consists in the intrapore growth of cyano-bridged networks at specific sites of the hybrid silica performed by consecutive coordination of M^{n+} (Fe^{2+}, Ni^{2+}, Fe^{3+}, Co^{2+}) and $[M'(CN)_m]^{3-}$ (M' = Fe^{3+}, Co^{3+} (m = 6), Mo^{5+} (m = 8)). Mesoporous SBA-15 and MCM-41 silicas types containing $-(CH_2)_2C_5H_4N$ functionalities $NC_5H_4(CH_2)_2SiO_{1.5}/xSiO_2$ (x = 7.3, 9.3 and 8.5) with pore diameters of 7.5, 5.3 and 3.4 nm were used (in the following labelled as **1a**, **1b** and **1c**). The growth of the nanoparticles into the silica was performed using the following typical procedure. The silica powder was consecutively treated first with a methanolic solution of M^{n+} and second with a methanolic solution of $[N(C_4H_9)_4]_3[M'(CN)_m]$ (M' = Fe, Co (m = 6), Mo (m = 8)). At each step of the treatment, the silica powder was thoroughly washed with methanol and dried *in vacuo*. Such procedure was repeated twice. A large range of nanocomposite materials containing $Ni^{2+}/[Fe(CN)_6]^{3-}$ **2a–c**, $Fe^{2+}/[Fe(CN)_6]^{3-}$ **3a–c**, $Fe^{3+}/[Mo(CN)_8]^{3-}$ **4a–c**, $Co^{2+}/[Co(CN)_6]^{3-}$ **5** and $Ni^{2+}/[Co(CN)_6]^{3-}$ **6** was obtained. The elemental analysis of nanocomposite materials **2–6** are given in Table 1 and the M/M′ atomic ratio extracted from elemental analysis is given in Table 2. For all the as-obtained nanocomposites the latter is close to 1. A further treatment of the obtained nanocomposite silica with $M^{n+}/[M'(CN)_m]^{3-}$ leads to the saturation of the silica matrices by the coordination polymer nanoparticles and may provoke the partial deposition of the bulk coordination polymers on the silica grain surface (Fig. 1S, ESI†).

Structural characteristics of the nanocomposites

The IR and Raman spectroscopies were performed on the nanocomposites **2–6** especially in the spectral window 2000–2300 cm^{-1}, *i.e.* in the vicinity of the CN stretching mode, which is a fingerprint of structural and electronic changes occurring in Prussian Blue analogous. The CN stretching frequency of a free CN^- ion is 2080 cm^{-1}, whereas upon coordination to a metal ion, it shifts to higher frequencies.[14] The IR spectra of the obtained nanocomposites **2–6**, listed in Table 2, show two characteristic absorption bands in the CN stretching region. The high-frequency bands can be attributed to the stretching of the CN ligand bridged between M^{2+} and M'^{3+} in M^{2+}–CN–M'^{3+} mode and the low-frequency bands can be assigned to the presence of the linkage isomer with M^{2+}–NC–M'^{3+} coordination mode, as it was reported for the bulk cyano-bridged coordination polymers.[15] Similar CN stretching frequencies can also be found in the spectra of the respective bulk cyano-bridged coordination polymers (Table 2). The Raman spectra of the studied nanocomposites **2–6** in the spectral region 2000–3000 cm^{-1} are dominated by two strong Raman signals. The first is centered in the vicinity of 2150 cm^{-1} except for **5** where it is found at 2197 cm^{-1} and the second is centered at *ca.* 2110 cm^{-1} except for **2**, where it is at 2070 cm^{-1} (Table 2). The Raman spectra can be interpreted in analogy with the IR absorption data, assigning the first band to the signal of the CN ligand bridged between M^{2+} and M'^{3+} in M–CN–M′ mode and the low-frequency bands to the presence of the linkage isomer with M–NC–M′ coordination mode. Similar signals were observed in Raman spectra of the bulk analogous also listed in Table 2. As expected, the IR spectra of the nanocomposites also present SiO_2 vibration bands at 1080, 948, 798 and 459 cm^{-1}, which are not observable by Raman spectroscopy.[14]

The electronic spectra of these nanocomposites show adsorption bands in the visible region corresponding to inter-metal charge-transfer bands from M to M′, which can also be found in the UV-Vis spectra of the bulk counterparts (Table 2).

Table 1 Elemental analyses of the nanocomposites **2–6**

Nanocomposite	M, wt%	M′, wt%	Si, wt%
2a	Ni, 1.07	Fe, 1.08	31.39
2b	Ni, 0.62	Fe, 0.65	26.52
2c	Ni, 0.66	Fe, 0.61	33.00
3a	Fe, 3.74	—	31.24
3b	Fe, 2.64	—	24.58
3c	Fe, 3.78	—	30.08
4a	Fe, 1.26	Mo, 1.23	32.38
4b	Fe, 1.59	Mo, 1.67	32.48
4c	Fe, 1.48	Mo, 1.54	31.85
5	Co, 6.79	—	24.21
6	Ni, 1.01	Co, 1.04	32.54

Table 2 Some relevant structural data for the nanocomposites **1–6** and their bulk counterparts

Sample	Composition: $M^{n+}/[M'(CN)_m]^{3-}$	M/M′ ratio[a]	Nanoparticle size/nm	IR: ν(CN)/cm^{-1}	Raman: ν/cm^{-1}	UV-Vis: λ/nm
2a	$Ni^{2+}/[Fe(CN)_6]^{3-}$	0.93	7.4 ± 1.9	2161, 2097	2152 (s), 2109 (w), 2074 (vw)	420
2b	$Ni^{2+}/[Fe(CN)_6]^{3-}$	0.95	5.1 ± 1.2	2165, 2098	2153 (s)	418
2c	$Ni^{2+}/[Fe(CN)_6]^{3-}$	1.08	2.0 ± 0.2	2163, 2100	2150 (s), 2111 (w), 2070 (vw)	420
	Bulk $Ni_3[Fe(CN)_6]_2$	1.5	—	2165, 2098	2146, 2099	400
3a	$Fe^{2+}/[Fe(CN)_6]^{3-}$	—	5.9 ± 0.8	2082, 2026	2143 (s), 2116 (w)	710
3b	$Fe^{2+}/[Fe(CN)_6]^{3-}$	—	3.5 ± 0.2	2089, 2026	2143 (s), 2117 (w)	696
3c	$Fe^{2+}/[Fe(CN)_6]^{3-}$	—	1.9 ± 0.1	2080, 2026	2153 (s), 2117 (w)	690
	Bulk $Fe_4[Fe(CN)_6]_3$	—	—	2078	2150	654
4a	$Fe^{3+}/[Mo(CN)_8]^{3-}$	1.02	7.1 ± 0.5	2153, 2110	2145 (s), 2047 (w)	680
4b	$Fe^{3+}/[Mo(CN)_8]^{3-}$	0.95	4.5 ± 0.1	2156, 2107	2155 (s), 2110 (w)	794
4c	$Fe^{3+}/[Mo(CN)_8]^{3-}$	0.96	2.4 ± 0.1	2157, 2112	2153 (s), 2117 (w)	810
	Bulk $Fe[Mo(CN)_8]$	1	—	2140	2160	820
5	$Co^{2+}/[Co(CN)_6]^{3-}$	—	6.2 ± 0.9	2174, 2127	2197 (s), 2107 (w)	410, 520
	Bulk $Co_3[Co(CN)_6]_2$	—	—	2173, 2138	2200, 2110	400, 510
6	$Ni^{2+}/[Co(CN)_6]^{3-}$	0.97	2.9 ± 0.6	2180, 2100	2142 (s), 2073 (w)	530, 730
	Bulk $Ni_3[Co(CN)_6]_2$	1.5	—	2187, 2141	2147, 2075	515, 725

[a] Extracted from elemental analyses.

Textural characteristics of the nanocomposites

In order to determine the effect of the insertion on the structure and porosity of the host matrix, the materials **2–6** were studied by transmission electronic microscopy (TEM). The TEM images of the pristine hybrid silica clearly show the hexagonal ordering of the pores (Fig. 2S, ESI†). The TEM measurements performed for the nanocomposites **2–6** indicate that in all cases, the hexagonal structure of the host materials is still retained. The TEM micrograph of the nanocomposite **2a** is given as an example in Fig. 1(a). No visible particles separated out of the surface of pores were observed. However, a distinctive signal for Ni and Fe was detected by energy dispersive spectroscopy (EDS) analyses with the atomic ratio Ni : Fe : Si of 1 : 1 : 32. As expected, no aggregates can be observed into the pores that is indicative of a homogeneous dispersion of the cyano-bridged polymer network in the silica matrix. The nanoparticles of coordination polymers can be clearly seen after removal of silica from the nanocomposite material using an HF treatment (extractive replicas). Fig. 1(b)–(d) show TEM micrographs performed on extractive replicas of the nanocomposites **2a**, **2b** and **2c** showing uniform in size and spherical in shape nanoparticles. All samples present relatively narrow size distribution centered at 7.4 ± 1.9 nm, 5.1 ± 1.2 and 2.0 ± 0.2 nm for **2a**, **2b** and **2c**, respectively (Table 2). These values are slightly smaller than the pore channel mean diameter of the respective host silicas of 7.5, 5.3 and 3.4 nm obtained from BET measurements (see Table 3). Obviously, the pore size of the silica matrix precludes further growth of the cyano-bridged network and the aggregation of the formed nanoparticles. The same tendency was observed for the TEM observations performed for the nanocomposites **3a–c** and **4a–c**. They also show decreasing of the size distribution of the nanoparticles with decreasing of the pore size of the respective host silica matrices demonstrating an evident correlation between the pore size of the silica and the size of the obtained nanoparticles. The average nanoparticle sizes of all the investigated nanocomposites, **2–6**, are summarized in Table 2.

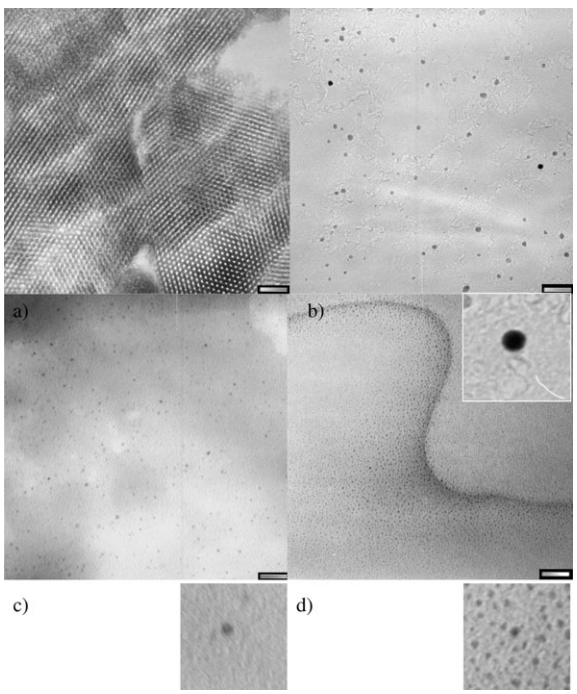

Fig. 1 TEM image of (a) the nanocomposite **2a** and the nanoparticles obtained after removal of silica using HF treatment (extractive replicas) for (b) **2a**, (c) **2b** and (d) **2c**. Scale bars = 50 nm. Insets show enlarged views (×10) of the nanoparticles.

The results of the TEM observations were substantiated by nitrogen physisorption and X-ray diffraction (XRD) analyses. The nitrogen physisorption isotherms and pore-size distributions at the desorption branch of the pristine hybrid silica of **1a** and the nanocomposite **2a** are shown in Fig. 2 as an example. The sample **1a** exhibits a typical adsorption–desorption isotherm of a mesoporous structure of type IV with an H1 hysteresis loop. A similar type of isotherm and mesoporosity is obtained for **2a**, which proves the preservation of the cylindrical pore system after intrapore growth of the cyano-bridged metallic coordination polymer. The amount of adsorbed nitrogen as well as the BET (Brunauer–Emmett–Teller) surface was reduced after formation of the coordination polymer

Table 3 Some relevant textural characteristics of the pristine hybrid mesoporous silicas and the nanocomposites **1–6**

Sample	S_{BET}/m^2 g^{-1}	V_p/cm^3 g^{-1}	Pore filling (%)	D_p[a]/nm	d_{100}/nm	d_{110}/nm	d_{200}/nm
1a	420	0.76	—	7.5	10.3	6.0	5.2
2a	320	0.57	25	7.6	10.2	6.1	5.3
3a	363	0.69	9	7.6	10.6	6.2	5.4
4a	301	0.62	18	7.6	10.4	6.2	5.4
5	298	0.63	18	7.2	7.1	5.2	4.0
6	325	0.56	25	7.2	9.2	5.3	4.7
1b	289	0.42	—	5.3	10.7	6.3	4.8
2b	243	0.355	41	3.7	8.1	—	—
3b	214	0.281	50	3.7	8.5	—	—
4b	223	0.309	52	4.2	8.9	4.8	—
1c	506	0.33	—	3.4	5.6	3.2	—
2c	109	0.087	78	2.0	4.5	—	—
3c	153	0.219	69	2.2	5.0	—	—
4c	169	0.113	64	2.2	5.0	—	—

[a] Calculated from the desorption branch of the nitrogen sorption isotherm by using the Barret–Joyner–Hellenda (BJH) method.

nanoparticles. Specific surface area along with the pore volume have been standardized *vs.* the pristine hybrid silica to check that the nanoparticles growth was not occurring only on the material surface, a conclusion that could be borne out by the sole consideration of the total weight. The decrease of the mesoporous volume standardized *vs.* the pristine hybrid silica **1a** and the decrease of the pore diameter, clearly demonstrate a filling of the pores with the guest species leading to the conclusion that the nanoparticles are formed inside the pores. The total pore volume calculated at $p/p_0 = 0.9$ is 0.76 cm^3 g^{-1} for the pristine hybrid silica **1a** and 0.57 cm^3 g^{-1} for **2a**. This indicates a degree of filling of the pores of *ca.* 25%. The observed nitrogen physisorption effects are well known in the literature for intrapore formation inside different host/guest systems.[16] The nitrogen physisorption isotherms and pore-size distributions at the desorption branch of the nanocomposites **2b** and **2c** and their respective pristine hybrid silicas **1b** and **1c** are shown in Fig. 3Sa and Sb (ESI†), respectively. They also present a filling of the pores with the cyano-bridged polymer nanoparticles with degrees of filling of *ca.* 40% for **2b** and of *ca.* 70% for **2c**. Specific surfaces, pore volumes and pore diameters obtained from nitrogen physisorption analyses of the nanocomposites **2–6** are gathered in Table 3. In all cases, a significant decrease in accessible surface and porosity in comparison to the respective host silica is observed for the obtained nanocomposites. It should also be noted that for all nanocomposites the degree of pore filling increases from *ca.* 10–20% for the nanocomposites obtained with the silica with pores of 7.5 nm, to *ca.* 40 and 70% for the nanocomposites obtained with the silica with pore diameters of 5.5 and 3.5 nm, respectively.

For all nanocomposites **2–6**, the XRD patterns in the range of 2θ 0.5–10° show a sharp peak due to the (100) reflection of the matrix along with, in the most cases, the (110) and (200) reflections clearly indicating that the mesoporous silica keeps its hexagonal structure (Table 3). The XRD pattern at 2θ 0.5–4° of the nanocomposite **2a** and its pristine host silica **1a** are shown in Fig. 3 as an example. A consecutive reduction of the X-ray peak intensities was observed in all nanocomposites with respect to the corresponding pristine hybrid silica. The

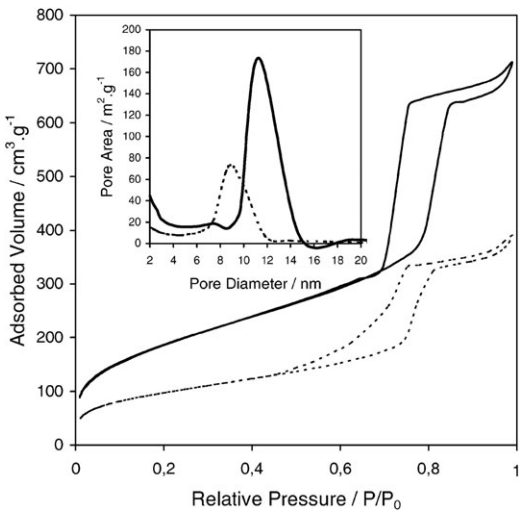

Fig. 2 Nitrogen adsorption/desorption isotherms for the pristine hybrid silica **1a** (solid line) and the nanocomposite **2a** (dashed line). Inset: BJH pore-size distribution calculated from the desorption branch for the pristine hybrid silica **1a** (solid line) and for the nanocomposite **2a** (dashed line).

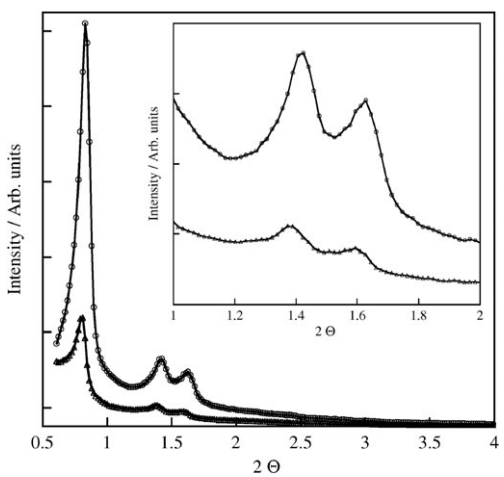

Fig. 3 Powder X-ray diffraction patterns within the range of 2θ (0.5–4°) for **1a** (○) and the nanocomposite **2a** (△). Inset: Magnification of the powder X-ray diffraction patterns showing the (110) and (200) reflections.

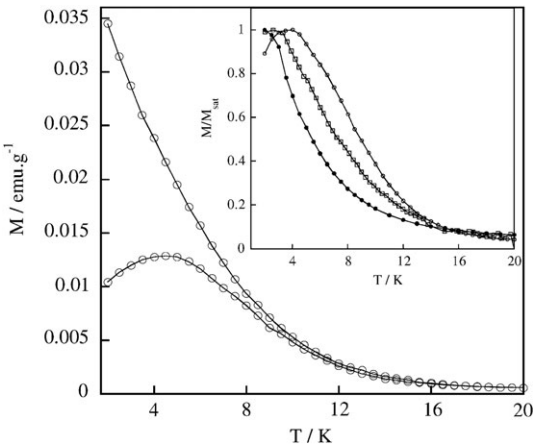

Fig. 4 Field-cooled and zero field-cooled magnetization (FC/ZFC) *vs.* temperature curves for the nanocomposite **2a** obtained by applying an external magnetic field of 10 Oe. Inset: Normalized zero field cooled (ZFC) magnetisation curves for the samples **2a** (○), **2b** (□) and **2c** (●). The applied magnetic field is 100 Oe.

intensity of the Bragg reflections originates from the difference in the scattering power between the silica walls and the empty pores. Due to the impregnation of the pores with the scattering material, the amount of scattering power within the pores is increased, resulting in overall loss of intensity due to phase cancellation between the pore walls and the guest species.[17]

Magnetic measurements

The magnetic measurements of the nanocomposite materials were performed by using dc and ac modes on the SQUID magnetometer working in the temperature range between 1.8 and 350 K. The zero field-cooled (ZFC)/field-cooled (FC) magnetization curves performed for the nanocomposite **2a** in the range of 2–20 K are shown in Fig. 4. The ZFC curve is obtained by recording the magnetization when the sample is heated under a field of 10 Oe after being cooled in zero field. The FC data were obtained by cooling the sample under the same magnetic field after the ZFC experiment and recording the change in sample magnetization with temperature. The ZFC/FC thermal irreversibility can be attributed to the blocking–unblocking process of the particle magnetic moment when thermal energy is varied,[18] or, for strongly interacting particle assemblies, to a spin-glass-like transition.[19] In both kinds of systems, the ZFC curve exhibits a maximum at a temperature $T_{max.}$ which in the two cases corresponds to the blocking temperature (T_B) of the nanoparticles with mean volume or to the freezing temperature (T_f), respectively.[19] For the sample **2a**, the ZFC curve shows a narrow peak with a maximum at 4.5 K and the FC curve increases as the temperature decreases and never reaches saturation. The FC and ZFC curves coincide at high temperatures and start to separate at 10.5 K, T_{sep}, which corresponds to the blocking of the largest particles. The closeness of T_{max} and the temperature of the ZFC/FC curves separation in this case confirms the presence of nanoparticles with a relatively narrow size distribution.

The ZFC/FC curves of samples **2b** and **2c** present a similar shape with average temperatures of maximum of 2.6 and <1.8 K, respectively (inset of Fig. 4, Table 4). The decrease of T_{max} for **2a**, **2b** and **2c** is qualitatively coherent with the decrease of the nanoparticles size from 7.4 ± 1.9 nm for **2a** to 5.1 ± 1.2 and 2.0 ± 0.2 for **2b** and **2c**, respectively (Table 2), which is expected for superparamagnetic systems.[20] The ZFC/FC magnetization curves of the nanocomposite **3a** in the range of 1.8–8 K present the same shape as those described above for **2a** and **2b** (Fig. 4S, ESI†); T_{max} was found at 2.25 K. For samples **3b** and **3c**, the peaks on the ZFC curves are lower that 1.8 K.

In fact the long-range ordering temperatures for the analogous bulk coordination polymers $Ni_3[Fe(CN)_6]_2{\cdot}13H_2O$ and $Fe_4[Fe(CN)_6]_3{\cdot}10.5H_2O$ determined as a first derivative of FC or ZFC curves are equal to 21 K and 5.5 K, respectively (Fig. 5S, ESI†). No temperature variation of the ZFC maximum was noted for the bulk samples prepared in different solvents (water, methanol or acetonitrile).

The irreversibility of the ZFC/FC curves was investigated in detail by using alternating current (ac) susceptibility measurements. The temperature dependence of the in-phase, χ' (absorptive), and out-of-phase, χ'' (dispersive), components of the ac susceptibility measured with no static field applied for frequencies from 1 to 1488 Hz for **2a**, are shown in Fig. 5(a) and (b). At 1 Hz, both χ' and χ'' responses present a peak at 8.27 and 7.01 K, respectively, which shifted toward higher temperatures as the frequency increases. Samples **2b** and **2c** show a similar frequency dependent behaviour but the peaks are all shifted toward lower temperatures with respect to sample **2a**. For instance, the peaks of χ' and χ'' of the sample **2b** are observed at 1 Hz at 5.86 and 4.35 K, respectively, and then shift toward higher temperatures with frequency (Fig. 5(c) and (d)). For **2c**, the maximum values of χ' and χ'' peaks are lower than 1.8 K, however a frequency dependent behaviour is clearly visible (Fig. 5(e) and (f)). The same situation was observed for the samples **3a** and **3b**, for which the maximum values of in-phase components of the ac susceptibility, χ', are clearly frequency dependent and the maximum values of its out-of-phase components, χ'', are lower than 1.8 K (Fig. 6S and 7S, ESI†). The frequency-dependent behaviour of these samples may be either attributed to: (i) the blocking

Table 4 Magnetic data of the nanocomposites **2a**, **b** and **3a**

			Arrhenius law		$T_g \neq 0$ K model			$T_g = 0$ K model			
Sample	T_{max}[a]/K	ϕ	(E_a/k_B)/K	τ_0, s	T_g/K	τ_0/s	$z\nu$	(E_a/k_B)/K	τ_0/s	$z\nu$	M_{sat}/emu g^{-1}
2a	4.50	0.07	276(8)	1.56×10^{-18}	4.5	3.43×10^{-3}	19	12770	1.60×10^{-7}	4	3.00
2b	2.60	0.06	134(3)	7.75×10^{-15}	2.93	1.09×10^{-3}	20	2061	1.59×10^{-6}	4	1.95
3a	2.25	0.045	109(9)	2.74×10^{-21}	1.4	1.82×10^{-7}	14	1895	3.65×10^{-4}	4	—

[a] Obtained as a maximum value of the ZFC curve.

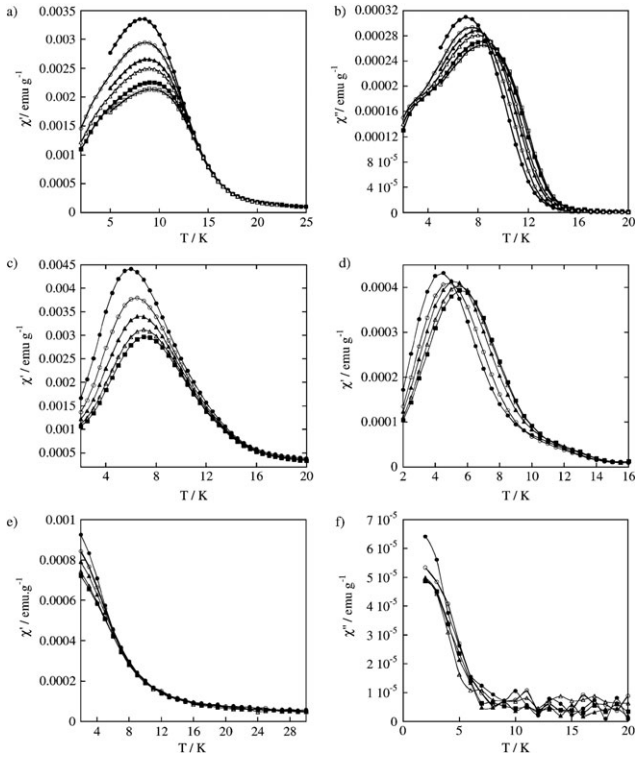

Fig. 5 Temperature dependence of in-phase, χ', component of the ac susceptibility of (a) **2a**, (c) **2b** and (e) **2c** with zero dc magnetic field and out-phase, χ'', component of the ac susceptibility of (b) **2a**, (d) **2b** and (f) **2c**. Frequencies: 1 Hz (●), 9.98 Hz (○); 125 Hz (▲), 499 Hz (△), 998 Hz (■) and 1498 Hz (□).

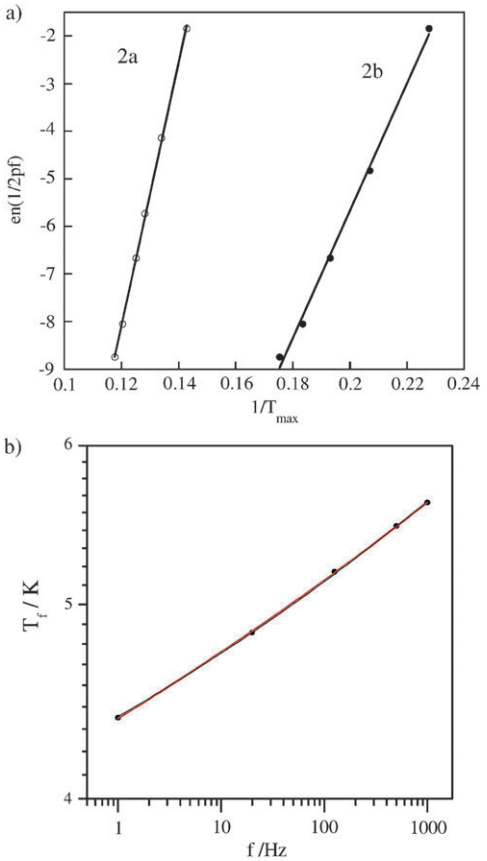

Fig. 6 (a) Thermal variation of the relaxation time according to the Arrhenius law for **2a** and **2b**. (b) Frequency dependence of the relaxation time according to the Vogel–Fulcher law for **2a** and **2b**.

process of non- or weakly-interacting superparamagnetic nanoparticles,[21] (ii) a spin-glass like transition, which may be caused by strong dipolar interparticle interactions and by randomness[19] or (iii) to an intraparticle spin glass-like regime due to the particle surface spin disorder.[19] Note that the temperature dependence of the ac susceptibility measured for the analogous bulk $Ni_3[Fe(CN)_6]_2{\cdot}13H_2O$ and $Fe_4[Fe(CN)_6]_3{\cdot}10.5H_2O$ shows no frequency dependence, as expected for compounds presenting long-range magnetic ordering (Fig. 8S, ESI†).

In order to understand the nature of low-temperature magnetic regime in these samples, we first evaluated the shift of the peak temperature (T_{max}) of χ'' for **2a** and **2b** by the parameter $\phi = (\Delta T_{max}/T_{max})/\Delta(\log f)$; ϕ is equal to 0.07 and 0.06 for **2a** and **2b** (Table 4), respectively. These values are intermediate between those typically obtained for superparamagnets (0.5–0.1) and canonical spin-glass (10^{-2}–10^{-3}) systems.[19]

Second, the temperature dependence of the relaxation time extracted from the maximum of the χ'' component of the ac susceptibility could be fit to an Arrhenius law, $\tau = \tau_0 \exp(E_a/k_B T)$, where E_a is the average energy barrier for the reversal of the magnetization, τ_0 is the attempt time and k_B is the Boltzmann constant. According to the Néel model this law governs the temperature dependence of the relaxation of the magnetization of non-interacting superparamagnetic systems.[22] The values of the energy barrier, E_a/k_B, and of the pre-exponential factor τ_0 are equal to 276(8) K and 1.56×10^{-18} s for **2a** and 134(3) K and 7.75×10^{-15} s for **2b** (Fig. 6, Table 4), respectively. The obtained values of τ_0 for both samples are much smaller than those observed for pure superparamagnetic systems (10^{-9}–10^{-12} s)[22] and have no physical meaning. From the obtained energy barrier values and using the average size obtained from TEM measurements, we get for the anisotropy constant K = 1.80 and 2.70×10^4 J m^{-3} for **2a** and **2b**, respectively. Given that for sample **3a** the maximum of χ'' are always lower than 1.8 K, the Arrhenius fit of the temperature dependence of the relaxation time was performed using the maximum of χ'. The so-obtained pre-exponential factor, $\tau_0 = 2.74 \times 10^{-21}$ s (Table 4) is similar to those obtained for **2a** and **2b**. Similar small values of τ_0 are often found for systems containing interacting metal or metal oxide nanoparticles[23] and are normally interpreted as the signature of a magnetic moments correlation introduced by considerable dipole–dipole interparticle interactions.

In order to investigate the possible presence of these interparticle interactions, the temperature dependence of the relaxation time was also fitted with the Vogel–Fulcher law, $\tau = \tau_0 \exp(E_a/k_B(T - T_0))$. This expression, which is used to describe the behaviour of structural glasses is, by analogy, also commonly used for magnetically interacting clusters.[24] Interparticle interactions are introduced by the additional parameter, T_0. The values of E_a/k_B, τ_0 and T_0 are equal to 261(20) K, 5.60×10^{-14} s and 0.15 ± 0.4 K for **2a** and 132(30)

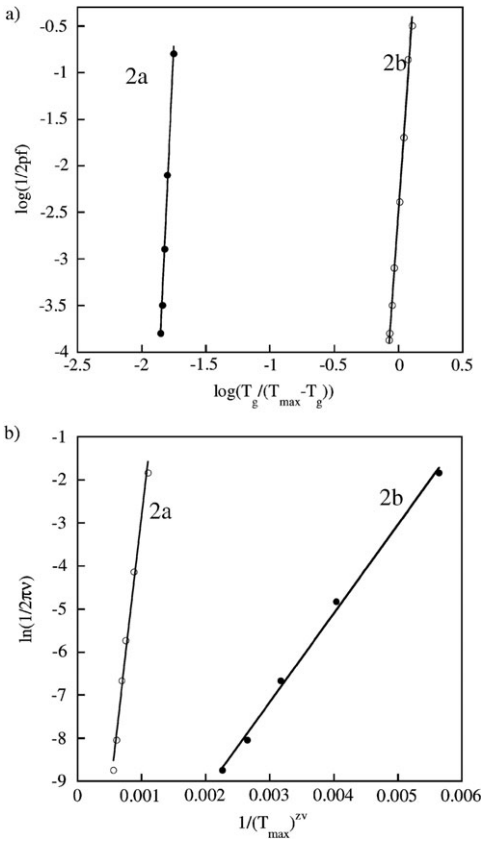

Fig. 7 (a) Relaxation time dependence on frequency fitted with the model of critical scaling law $\tau = \tau_0[T_g/(T_{max} - T_g)]^{z\nu}$ for **2a** and **2b**. (b) Relaxation time dependence on frequency fitted with the model of critical scaling law $\tau = \tau_0 \exp(E_a/k_B T_g^{z\nu})$ for **2a** and **2b**.

K, 4.75×10^{-14} s and 0.11 ± 0.6 K for **2b**, respectively (Fig. 6(b)). In this way τ_0 values are larger than those obtained with the previous fit, but still smaller than 10^{-12} s. In addition, the small values of T_0 along with the large error bars suggest that interparticle interactions in these systems are weak.

We further verified if the dynamics of these samples would exhibit critical slowing down, as observed in canonical spin-glass systems. Two cases were considered depending on whether the transition temperature has a finite value or not.[25] In the first case, an equilibrium ordered phase occurs at a finite critical temperature, $T_g \neq 0$ K, and the relaxation time dependence on frequency can be fitted by the conventional critical scaling law of the spin dynamics, $\tau = \tau_0[T_g/(T_{max} - T_g)]^{z\nu}$, and $T_{max} = T_g[1 + (\tau_0 f)^{1/z\nu}]$, where T_g is the glass temperature, f is the frequency and $z\nu$ is a critical exponent.[23,25] The best fits give $T_g = 4.5$ K, $\tau_0 = 3.43 \times 10^{-3}$ s and $z\nu = 19$ for **2a** and $T_g = 2.1$ K, $\tau_0 = 1.09 \times 10^{-3}$ s and $z\nu = 20$ for **2b** (Fig. 7(a), Table 4). Similar results were obtained for sample **3a** (Table 4). The obtained $z\nu$ values lie out of the range 4–12 expected for classical spin glass systems; the same holds for τ_0 which should be in the range 10^{-7}–10^{-12} s.[19] In the second case, the transition temperature occurs at $T_g = 0$ K and the frequency dependence of the relaxation time can be described by a generalized Arrhenius law $\tau = \tau_0 \exp(E_a/k_B T_{max}^{z\nu})$. [23a,26] The frequency dependence of τ fitted with this law gives values of $z\nu = 4$, $\tau_0 = 1.6 \times 10^{-7}$ s, $E_a/k_B = 12770$ K for **2a** and $z\nu = 4$, $\tau_0 = 1.59 \times 10^{-6}$ s, $E_a/k_B = 2061$ K for **2b**. The results obtained for the samples **2a**, **b** and **3a** are summarized in Table 4. For all samples τ_0 is larger than that in conventional spin-glasses ($\sim 10^{-13}$ s), but close to what observed in the case of cluster-spin glass systems ($\sim 10^{-6}$–10^{-11} s) especially when the clusters are nanometric,[27] as in our case. However, the obtained energy barriers, in all cases situated in the 1200–2000 K range, are unrealistically too large, suggesting, that also this model is not appropriate to describe our systems.

The field dependence of the magnetization measured for **2a** and **2b** at 1.8 K shows that the saturation magnetisation of the nanocomposites at 50 kOe are equal to 3.0 emu g^{-1} (771 emu mol^{-1}) and 1.95 emu g^{-1} (519 emu mol^{-1}), respectively (Table 4). These values correspond to the expected values for 5.0 and 3.1% of 16 755 emu mol^{-1} ($3\mu_B$) calculated for the {NiFe} unit with ferromagnetic Ni^{2+}–Fe^{3+} interactions through the cyano bridge. These results are in agreement with those obtained by elemental analysis. A very small hysteresis loops with coercive field of 80 Oe were observed for these two samples. In the case of the **2c**, **3a–3c** samples, the saturation of the magnetisation was not yet attained at 1.8 K with a field of 50 kOe.

In summary, contrarily to what observed for the corresponding bulk coordination polymers, our samples exhibit a low-temperature slow dynamics which, in principle, may originate from different magnetic regimes: the superparamagnetic regime is due to the distribution of relaxation times originating from the anisotropy energy barriers. In this case, the magnetic moment of each particle relaxes according to its individual energy barrier that depends on the magnetic anisotropy constant and the nanoparticle volume. Therefore, a distribution of particle volumes results in a distribution of energy barriers and blocking temperatures. However the fit to the Arrhenius law clearly shows that the observed behaviour is not purely superparamagnetic. On the contrary the cooperative spin-glass-like dynamics, usually observed in dense magnetic nanoparticles systems, results in the presence of a complex relative energy minima configuration instead of a unique ground state. The local energy barriers between these configurations are low, enabling a constant development toward equilibrium, but resulting in the inability to reach it. The comparison of different models appropriate for systems with relatively strong interparticle interactions, (Vogel–Fulcher law and two critical slowing down models) permits also to exclude this hypothesis. Moreover the Vogel–Fulcher law fit shows the presence of negligible interparticle interactions. These results are supported by the TEM measurements where no evidence aggregated particles was obtained.

Since the mesostructured silica provides an insulating matrix and since the particles are not agglomerated, the possible interparticle magnetic interactions are of dipole–dipole type. Assuming a homogeneous dispersion of the spherical nanoparticles into the silica matrix, the mean interaction energy between two neighbouring particles can be estimated from eqn (1):

$$E_{d-d} = \frac{\mu_0}{4\pi} M_s^2 V_m \varepsilon = \frac{\mu_0}{24} M_s^2 d_m^3 \varepsilon, \qquad (1)$$

where M_s is the saturation magnetization of the nanoparticles, μ_0 is the magnetic permeability ($4\pi \cdot 10^{-7}$ N A^{-2}), V_m and d_m are the median particle volume and diameter, respectively and ε is the volume concentration of particles.[28] Using the low-temperature value of the saturation magnetization at 2 K (Table 4, ESI†), this expression gives $E_{d-d}/k_B \approx 1$ K for the sample **2a**. This value, even if not negligible, is lower than the energy barrier obtained from ZFC curve ($\sim$100 K, Table 4). This suggests that the interparticle dipolar interactions are strong enough to modify the magnetic response from that expected for non-interacting superparamagnetic particles but, on the other hand, are too weak to provide a collective state with a spin-glass-like behavior, producing an intermediate dynamics.[28]

On the other hand, on the basis of these results it can be also argued that the dynamics observed in our systems arise from an intraparticle spin-glass behaviour mainly caused by spin-frustration inside the nanoparticles. Indeed for ultrafine nanoparticles (<7 nm) the surface-to-volume ratio is very large and the surface contribution should have an important role on the magnetic properties of nanoparticles.[29,30] The structural disorder at the surface might be the reason for the lack of full alignment of the spins in the nanoparticles and therefore of the spin frustration, responsible for the observed spin-glass like dynamics.

Conclusion

In conclusion, the concept of using the well-organized pore systems of mesoporous hybrid silica as nanoreactors appears to be a promising alternative for the growth and the organization of coordination polymer nanoparticles. A large range of size controlled cyano-bridged coordination polymer nanoparticles $M^{n+}/[M'(CN)_m]^{3-}$ (where M^{2+} = Ni, Fe, Co and M′ = Fe, Co (n = 6); Mo (n = 8)) with controlled stoichiometry was obtained by using mesostructured hybrid silica hosts of different sizes (3.4, 5.3 and 7.5 nm) containing $-(CH_2)_2C_5H_4N$ functional anchoring groups. We obtained spherical and uniform-sized nanoparticles with relatively narrow size distribution situated exclusively inside the silica pores.

The first point to note is that the covalent anchorage of the nanoparticle precursor metal salts inside the functionalized silica plays an important role in the fabrication of the coordination polymer nanoparticles. The initial dispersion of the pyridine bonding sites of the hybrid silica avoids both aggregation and extrusion of the formed coordination polymer nanoparticles and allows control of their dispersion. Indeed, attempts to prepare the same coordination polymer nanoparticles by using unfunctionalized mesoporous silica with similar pore sizes do not allow insertion of coordination polymers into the silica pores.[13]

Another important point to note is that the size of these nanoparticles is in a good correlation with the pore size of the hybrid silica indicating that the matrix governs the growth of the coordination polymer nanoparticles networks precluding their further growth and allowing the synthesis of nanoparticles with different controlled sizes.

The magnetic measurements performed on these nanocomposites by using both dc and ac modes confirm the formation of the coordination polymer nanoparticles. The decrease of T_{max} observed for nanoparticles with the same composition but with different size is in correlation with the TEM measurements. The dynamic analysis in these systems reveals that no pure superparamagnetic regime of the nanoparticles is observed. On the other hand, the fits of the experimental data to different models appropriate for spin-glass like systems are unsatisfactory. These results, together with the estimation of the mean dipolar interaction energy between two neighbouring particles, suggest that the latter can produce deviations from the Néel model for non-interacting nanoparticles, but can not generate a collective state with a interparticle spin-glass like behaviour. Alternatively the presence of spin frustration on the surface of the nanoparticles may by responsible of the presence of a intraparticle spin-glass like behaviour in our systems.

Experimental

Synthesis

All of the chemical reagents used in these experiments were of analytical grade.

Synthesis of hybrid mesostructured silicas 1a–c. SBA-15 type silicas **1a** and **1b** with pore diameters of 7.5 and 5.3 nm were synthesised using a triblock copolymer (P123) as surfactant as previously described.[31] A mesostructured silica MCM-41, **1c**, with a pore diameter of 3.4 nm was synthesised by using CTAB as surfactant as previously described.[32] The grafting of the organic functionality $-(CH_2)_2C_5H_4N$ into the silica pores was performed by refluxing in toluene the pristine silica in the presence of the organic compound $(CH_3O)_3Si(CH_2)_2C_5H_4N$ overnight.[33] As a result, the hybrid silicas $NC_5H_4(CH_2)_2SiO_{1.5}/xSiO_2$ (x = 7.7 for **1a**, 9.3 for **1b** and 8.5 for **1c**) were obtained. The content of pyridine groups was determined by elemental analysis. Elem. anal. (%): found for **1a**: Si, 35.13; N, 2.27 *i.e.* organic loading 1.61 mmol g^{-1}; for **1b**: Si, 34.94; N, 1.62 *i.e.* organic loading 1.39 mmol g^{-1} and for **1c**: Si, 32.71; N, 1.38 *i.e.* organic loading 1.49 mmol g^{-1}.

Intrapore growth of cyano-bridged metallic coordination polymer nanoparticles

The intrapore growth of hetero- and homo-metallic cyano-bridged coordination polymer nanoparticles was performed by using the following procedure. First, a hybrid silica powder of **1** (75 mg) was added to a 10^{-2} M solution of $[M(H_2O)_6]Cl_2$ (M = Ni for **2**, **6**, Fe for **3**, Co for **5**) or $[Fe(H_2O)_6]Cl_3$ for **4** in methanol. The mixture was stirred overnight at room temperature. After filtration, the powder was thoroughly washed several times with methanol and dried at room temperature for 24 h *in vacuo*. Secondly, the so-obtained powder was added to a 10^{-2} M methanolic solution of the appropriate complex $[N(C_4H_9)_4]_3[Fe(CN)_6]$[34] for **2** and **3**, $[N(C_4H_9)_4]_3[Mo(CN)_8]$[35] for **4**, $[N(C_4H_9)_4]_3[Co(CN)_6]$[36] for **5** and **6**. The mixture was stirred for 48 h, the powder was filtered, thoroughly washed with methanol and dried *in vacuo*. Such consecutive treatments with metal salts and cyanometallate precursors were repeated again. The elemental analyses of the nanocomposites **2–6** are given in Table 1.

Physical measurements

IR spectra were recorded on a Perkin Elmer 1600 spectrometer with a 4 cm^{-1} resolution. UV-Vis spectra were recorded in KBr disks on a Cary 5E spectrometer. Elemental analyses were performed by the Service Central d'Analyse (CNRS, Vernaison, France). The samples were heated at 3000 °C under He. Oxygen was transformed in CO and detected by using an IR detector. Powder X-ray diffraction patterns were measured on a PanAnalytical diffractometer equipped with an ultra-fast X'celerator detector X'pert Pro with Nickel-filtered copper radiation (1.5405 Å). The measurement parameters are: step-size, 0.01671; counting time, 60 s. Magnetic susceptibility data were collected with a Quantum Design MPMS-XL SQUID magnetometer working in the temperature range of 1.8–300 K and the magnetic field range of 0–50 kOe. Ac susceptibility measurements were performed with an home-made probe inserted in an Oxford cryostat, operating in the 20–25 000 Hz range. The data were corrected for the sample holder and the diamagnetism contributions calculated from the Pascal's constants.[37]

Samples for transmission electron microscopy (TEM) measurements were prepared using extractive replicas or ultramicrotomy techniques and then deposited on copper grids. TEM measurements were carried out at 100 kV with a microscope JEOL 1200 EXII. The nanoparticles size distribution histograms were determined using enlarged TEM micrographs taken at magnification of ×50 K. A large number of nanoparticles (400–600) were counted in order to obtain a size distribution with good statistics.

Acknowledgements

The authors thank Dr Arie van der Lee (IEM, UMR 5635, Montpellier, France) for XRD measurements and Mme. Corine Rebeil (UM2, Institute Charles Gerhardt Montpellier, France) for magnetic measurements. The authors also thank the CNRS, the Université Montpellier II and the network of excellence MagManet (FP6-NMP3-CT-2005-515767) for financial support. C. L. thanks Marie Curie fellowship associated to the EC "QuEMOLNa" project, MRTN-eT-2003 504880.

References

1 M. Drillon and J. Miller, *Magnetism: Molecules to Materials IV*, Wiley-VCH, Weinheim, 2005.
2 (*a*) R. Koncki, *Crit. Rev. Anal. Chem.*, 2002, **32**, 79; (*b*) S. Ayrault, C. Loos-Neskovic, M. Fedoroff and E. Garnier, *Talanta*, 1994, **41**, 1435; (*c*) L. Roberts, *Science*, 1987, **238**, 1028; (*d*) D. Wenker, B. Spiess and P. Laugel, *Food Addit. Contam.*, 1990, **7**, 375; (*e*) H. J. Byker, in *Electrochromic Materials II*, ed. K. C. Ho and D. A. MacArthur, The Electrochemical Society, Pennington, NJ, 1994, vol. 94–2, p. 3; (*f*) S. Ferlay, T. Mallah, R. Ouahes, P. Veillet and M. Verdaguer, *Nature*, 1995, **378**, 701.
3 (*a*) O. Hatlevik, W. E. Buschmann, J. Zhang, J. L. Manson and J. S. Miller, *Adv. Mater.*, 1999, **11**, 914; (*b*) S. M. Holmes and G. S. Girolami, *J. Am. Chem. Soc.*, 1999, **121**, 5593; (*c*) B. G. Morin, C. Hahm, A. J. Epstein and J. S. Miller, *J. Appl. Phys.*, 1994, **75**, 5782; (*d*) J. S. Miller, *Adv. Mater.*, 1994, **6**, 322; (*e*) S. Ferlay, T. Mallah, R. Ouahès, P. Veillet and M. Verdaguer, *Inorg. Chem.*, 1999, **38**, 229; (*f*) W. E. Buschmann, S. C. Paulson, C. M. Wynn, M. Girtu, A. J. Epstein, H. S. White and J. S. Miller, *Adv. Mater.*, 1997, **9**, 645; (*g*) W. R. Entley and G. S. Girolami, *Science*, 1995, **268**, 397; (*h*) S. Ferlay, T. Mallah, R. Ouahès, P. Veillet and M. Verdaguer, *Nature*, 1995, **378**, 701; (*i*) V. Gadet, T. Mallah, I. Castro and M. Verdaguer, *J. Am. Chem. Soc.*, 1992, **114**, 9213; (*j*) T. Mallah, S. Thiébaut, M. Verdaguer and P. Veillet, *Science*, 1993, **262**, 1554; (*k*) O. Sato, T. Iyoda, A. Fujishima and K. Hashimoto, *Science*, 1996, **271**, 49; (*l*) S. Ohkoshi and K. Hashimoto, *J. Am. Chem. Soc.*, 1999, **121**, 10591.
4 E. Dujardin and S. Mann, *Adv. Mater.*, 2004, **16**, 1125.
5 G. Schmid, *Nanoparticles: From Theory to Application*, Wiley-VCH, Weinheim, 2004.
6 M.-I. Baraton, *Synthesis, Functionalization and Surface Treatment of Nanoparticles*, American Scientific Publishers, Stevenson Ranch, CA, 2003.
7 (*a*) S. Vaucher, M. Li and S. Mann, *Angew. Chem., Int. Ed.*, 2000, **39**, 1793; (*b*) S. Mann, J. Fielden, M. Li, E. Dujardin and S. Mann, *Nano Lett.*, 2002, **2**, 225.
8 L. Catala, T. Gacoin, J.-P. Boilot, E. Rivier, C. Paulsen, E. Lhotel and T. Mallah, *Adv. Mater.*, 2003, **15**, 826.
9 (*a*) T. Uemura and S. Kitagawa, *J. Am. Chem. Soc.*, 2003, **125**, 7814; (*b*) D. M. DeLongchamp and P. T. Hammond, *Adv. Funct. Mater.*, 2004, **14**, 224; (*c*) L. Catala, A. Gloter, O. Stephan, G. Rogez and T. Mallah, *Chem. Commun.*, 2006, 1018; (*d*) D. Brinzei, L. Catala, N. Louvain, G. Rogez, O. Stéphan, A. Gloter and T. Mallah, *J. Mater. Chem.*, 2006, **16**, 2503.
10 (*a*) Y. Guari, J. Larionova, K. Molvinger, B. Folch and Ch. Guérin, *Chem. Commun.*, 2006, 2613; (*b*) J. M. Domingez-Vera and E. Colacio, *Inorg. Chem.*, 2003, **42**, 6983.
11 (*a*) P. Zhou, D. Xue, H. Luo and X. Chen, *Nano Lett.*, 2002, **2**, 845; (*b*) J. G. Moore, E. J. Lochner, C. Ramsey, N. S. Dalal and A. E. Stiegman, *Angew. Chem., Int. Ed.*, 2003, **42**, 2741.
12 G. Clavel, J. Larionova, Y. Guari and Ch. Guérin, *Chem.–Eur. J.*, 2006, **12**, 3798.
13 G. Clavel, Y. Guari, J. Larionova and Ch. Guérin, *New J. Chem.*, 2005, **29**, 275.
14 K. Nakamoto, *Infrared and Raman Spectra*, John Wiley and Sons Inc, New York, 1986.
15 D. F. Shriver, S. A. Shriver and S. E. Anderson, *Inorg. Chem.*, 1965, **4**, 725.
16 R. Köhn and M. Fröba, *Catal. Today*, 2001, **68**, 227.
17 (*a*) W. Hammond, E. Prouzet, S. D. Mahanti and T. Pinnavaia, *Microporous Mesoporous Mater.*, 1999, **27**, 19; (*b*) M. Froba, R. Köhn and G. Bouffaud, *Chem. Mater.*, 1999, **11**, 2858; (*c*) F. J. Brieler, M. Fröba, L. Chen, P. J. Klar and W. Heimbrodt, *Chem. Eur. J.*, 2002, **8**, 185; (*d*) F. J. Brieler, P. Grundmann, M. Fröba, L. Chen, P. J. Klar, W. Heimbrodt, H.-A. K. von Nidda, T. Kurz and A. Loidl, *J. Am. Chem. Soc.*, 2004, **126**, 797.
18 L. Nèel, *Ann. Geophys.*, 1949, **60**, 661.
19 J. A. Mydosh, *Spin Glasses*, Taylor and Francis, Washington, DC, 1993.
20 S. D. Tiwari and K. P. Rajeev, *Phys. Rev. B*, 2005, **72**, 104433.
21 J. L. Dormann, L. Bessais and D. Fiorani, *J. Phys. C*, 1988, **21**, 2015.
22 L. Nèel, *Adv. Phys.*, 1955, **4**, 191.
23 (*a*) C. Djurberg, P. Svedlindh, P. Nordblad, M. F. Hansen, F. Bodker and S. Morup, *Phys. Rev. Lett.*, 1997, **79**, 5154; (*b*) G. Balaji, G. Wilde, J. Weissmuller, N. S. Gabhiye and V. K. Sankaranarayanan, *Phys. Status Solidi B*, 2004, **241**, 1589.
24 M. A. Girtu, *J. Optoelectron. Adv. Mater.*, 2002, **4**, 85.
25 C. Dekker, A. F. M. Arts, H. W. De Wijn, A. J. Van Duyneveldt and J. A. Mydosh, *Phys. Rev. B*, 1989, **40**, 11243.
26 N. Bontemps, J. Rajchenbach, R. V. Chamberlin and R. Orbach, *Phys. Rev. B*, 1984, **30**, 6514.
27 (*a*) M. D. Mukadam, S. M. Yusuf, P. Sharma, S. K. Kulshreshtha and G. K. Dey, *Phys. Rev. B*, 2005, **72**, 174408; (*b*) G. Balaji, G. Wilde, J. Weissmuller, N. S. Gabhiye and V. K. Sankaranarayanan, *Phys. Status Solidi B*, 2004, **241**, 1589; (*c*) C. Djurberg, P. Svedlindh, P. Nordblad, M. F. Hansen, F. Bødker and S. Mørup, *Phys. Rev. Lett.*, 1997, **79**, 5154.
28 T. Jonsson, P. Nordblad and P. Svedlindh, *Phys. Rev. B*, 1998, **57**, 497.
29 E. Tronc, D. Fiorani, M. Noguès, A. M. Testa, F. Lucari, F. D'Orazio, J. M. Grenèche, W. Wernsdorfer, N. Galvez, C. Chanéac, D. Mailly and J. P. Jolivet, *J. Magn. Magn. Mater.*, 2003, **262**, 6.

30 D. Bonacchi, A. Caneschi, D. Dorignac, A. Falqui, D. Gatteschi, D. Rovai, C. Sangregorio and R. Sessoli, *Chem. Mater.*, 2004, **16**, 2016.
31 (*a*) D. Zhao, J. Feng, Q. Huo, N. Melosh, G. H. Fredrickson, B. F. Chmelka and G. D. Stucky, *Science*, 1998, **279**, 548; (*b*) D. Zhao, Q. Huo, J. Feng, B. F. Chmelka and G. D. Stucky, *J. Am. Chem. Soc.*, 1998, **120**, 6024.
32 (*a*) C. T. Kresge, M. E. Leonowicz, W. J. Roth, J. C. Vartuli and J. S. Beck, *Nature*, 1992, **359**, 710; (*b*) J. S. Beck, J. C. Vartuli, W. J. Roth, M. E. Leonowicz, C. T. Kresge, K. D. Schmitt, C.-T.-W. Chu, D. H. Olsen, E. W. Sheppard, S. B. McCullen, J. B. Higgins and J. L. Schlenker, *J. Am. Chem. Soc.*, 1992, **114**, 10834.
33 (*a*) L. Mercier and T. J. Pinnavaia, *Adv. Mater.*, 1997, **9**, 500; (*b*) A. Cauvel, G. Renard and D. Brunel, *J. Org. Chem.*, 1997, **62**, 749; (*c*) A. M. Liu, K. Hidajat, S. Kawi and D. Y. Zhao, *Chem. Commun.*, 2000, 1145; (*d*) R. J. P. Corriu, E. Lancelle-Beltran, A. Mehdi, C. Reye, S. Brandes and R. Guilard, *J. Mater. Chem.*, 2002, **12**, 1355.
34 P. K. Mascharah, *Inorg. Chem.*, 1986, **25**, 15.
35 B. J. Corden, J. A. Cunningham and R. Eisenberg, *Inorg. Chem.*, 1970, **9**, 1355.
36 The synthesis of $[N(C_4H_9)_4)_3][Co(CN)_6]$ was adapted from the synthesis of $[N(C_4H_9)_4]_3[Mo(CN)_8]$ given in ref. 31.
37 E. A. L. Boudreaux and N. Mulay, *Theory and Applications of Molecular Paramagnetism*, John Wiley & Sons, New York, 1976.

